Advances in Geo-Energy Research

Vol. 6, No. 4, p. 314-323, 2022

Original article

Image feature recognition and gas permeability prediction of Gaomiaozi bentonite based on digital images and machine learning

Jiangfeng Liu[1,2], Shijia Ma[1], Wanqing Shen[3], Junping Zhou[4], Yi Hong[2]*

[1]*State Key Laboratory for Geomechanics and Deep Underground Engineering, China University of Mining and Technology, Xuzhou 221116, P. R. China*

[2]*Key Laboratory of Offshore Geotechnical and Material Engineering of Zhejiang Province, Zhejiang University, Hangzhou 310058, P. R. China*

[3]*LaMcube, FRE2016, CNRS, University of Lille, Lille 59000, France*

[4]*State Key Laboratory of Coal Mine Disaster Dynamics and Control, Chongqing University, Chongqing 400044, P. R. China*

Keywords:
Gaomiaozi bentonite
permeability
digital image
extreme learning machine

Cited as:
Liu, J., Ma, S., Shen, W., Zhou, J., Hong, Y. Image feature recognition and gas permeability prediction of Gaomiaozi bentonite based on digital images and machine learning. Advances in Geo-Energy Research, 2022, 6(4): 314-323.
https://doi.org/10.46690/ager.2022.04.06

Abstract:
Gas permeability, which is measured mainly through gas permeability experiments, is a critical technical index in many engineering fields. In this study, permeability is firstly calculated based on information from a digital image and an improved permeability prediction model. The calculated results are experimentally verified. Subsequently, a self-developed image-processing program is used to extract feature parameters from a scanning electron microscopy image. Meanwhile, an extreme learning machine algorithm is used to input the image feature parameters obtained using the image-processing program into the extreme learning machine algorithm for machine learning. Additionally, we compare several typically used machine learning algorithms, which confirmed the reliability and accuracy of our algorithm. The best activation function can be obtained by comparing the predicted permeability using an appropriate number of neuron nodes. Experimental results show that the program can accurately identify the features of the microscopy image. Combining the program with an extreme learning machine neural network algorithmgas permeability results to be obtained with high accuracy. This method yields good predictions of permeability in certain cases and has been adapted to other geomaterials.

1. Introduction

Gas permeability is a key technical indicator in many other geological engineering fields, such as deep energy extraction (e.g., coal bed methane, shale gas, and natural gas hydrate extraction), and deep energy and waste storage (e.g., underground oil and gas storage, high-level radioactive waste (HLRW) storage, and CO_2 deep geological storage) (Mazarei et al., 2019; Carbonell et al., 2019; Alafnan, 2022). Therefore, methods for obtaining the gas permeability of geomaterials in these engineering geological fields have been investigated extensively. The typical method for predicting permeability involves indoor experimental testing, on-site sampling, and returns the results to a laboratory for evaluation. However, this method requires on-site core drilling and sampling, which typically diminish the integrity of the entire engineering body, and yields a low testing efficiency.

The characteristics of gas migration in geomaterials are primarily determined by their pore structure characteristics (e.g., porosity, size, and distribution of pores and throats) and the connectivity of the pore network (Huang et al., 2021). The development of scanning technology has enabled in situ scanning for acquiring digital images of samples at different locations without damaging the engineering structure. The

Yandy Scientific Press

*Corresponding author.
E-mail address: jeafliu@hotmail.com (J. Liu); ts19030001a31@cumt.edu.cn (S. Ma); Wanqing.Shen@polytech-lille.fr (W. Shen); zhoujp1982@sina.com (J. Zhou); yi_hong@zju.edu.cn (Y. Hong).

Received March 26, 2022; revised April 30, 2022; accepted May 15, 2022; available online May 17, 2022.

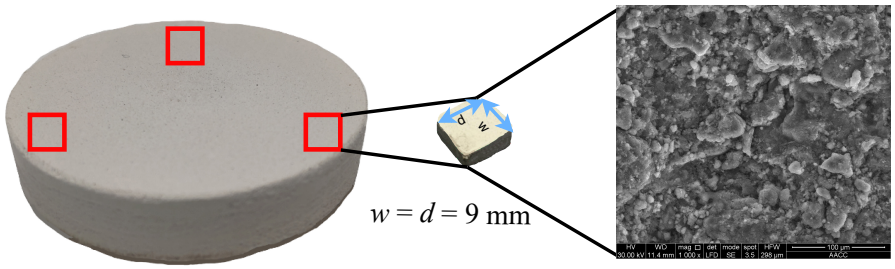

Fig. 1. Scanning sample acquisition.

pore structure morphology of geomaterials can be directly observed using digital imaging technology (Gebrenegus et al., 2011). Some scholars have used digital images to directly observe the microstructure characteristics of geomaterials, perform quantitative characterization, and determine the relationship between permeability and pore structure based on relative theories (Dou et al., 2021; Zhao et al., 2022). However, the process of digital image based on the penetration rate is complicated, and the technical requirements are relatively high. Generally, a significant amount of time is required to obtain permeability based on an image, and the processing efficiency is relatively low.

Owing to the development of artificial neural networks, neural network models have been applied to solve inverse problems. For example, scholars have used artificial neural networks to determine reservoir parameters to assess the production capacity of wells (Ahmadi et al., 2017; Xiao and Hugh, 2018). Computer vision and neural networks were used to acquire microscopy images, manually construct annotated big data samples, and train those samples to identify, extract, or count cracks, pores, or particles. Geological/geotechnical parameters are essential in engineering surveys. Scholars have attempted to obtain these parameters rapidly and accurately using machine learning (ML), which significantly improved efficiency (Arif et al., 2012; Taha et al., 2018; Bahmed et al., 2019; Hossein et al., 2021). Existing ML prediction algorithms include support vector regression (SVR), decision trees, Gaussian process regression (GPR) models, and extreme learning machine (ELM) (Dominguez-Olmedo et al., 2020; Shokouhi et al., 2021). Each method exhibits its own characteristics; for example, the decision tree is a classic binary-tree-based principle construction model. However, it overfits easily, and the structure of the tree changes significantly when only a few changing samples is involved. The GPR model is a nonparametric model that uses a Gaussian process to perform a priori regression analyses of data; it is suitable for datasets with low dimensions and small sample counts. Although the GPR model offers high accuracy, its parameters are difficult to adjust.

Inspired by these studies, we combined image processing with neural networks. First, we developed a digital image processing system to obtain the relevant characteristic parameters of the image. Subsequently, we utilized digital image processing technology to calculate the permeability of the image. Earlier studies indicated that permeability calculation based on digital images yielded results similar to those of physical experiments. A sample-learning database can be established using the image parameters and corresponding permeability values, followed by ML based on the ELM algorithm. This method allows a significant amount of image processing and ML to be performed rapidly and yields accurate results. Hence, it is suitable for the nondestructive in situ quantitative evaluation of engineering structures (e.g., to evaluate the sealing performance evolution of the bentonite barrier in the HLRW repository).

2. Methodology

2.1 Digital image quantitative characterization and permeability prediction

2.1.1 Digital image quantitative characterization

(1) Experimental materials

Gaomiaozi (GMZ) bentonite was selected as the optimal buffer material from a high-level radioactive waste repository in China (Xu et al., 2020). Initially, a compacted GMZ bentonite sample was loaded onto a triaxial cell to perform gas permeability tests. Subsequently, three 9 mm × 9 mm specimens were selected from different sections of the sample to closely represent the pore structure of the entire sample. This was performed to avoid images acquired in the same section that were not representative owing to the heterogeneity of the geomaterial. Additionally, because the bentonite specimens were pressed, the homogeneity of the digital image showing the pore structure should be greater than that of other geological materials. Nine specimens obtained from three samples were subjected to scanning electron microscopy (SEM), which was performed at the Modern Analysis and Computing Center of China University of Mining and Technology. The selected image was magnified 1,000 times (Fig. 1).

(2) Image enhancement

The actual obtained image can be either overly bright or dark. The brightness of the image can be adjusted using grayscale mapping to restore it to the normal brightness level by adding or subtracting a value from the original pixel grayscale value. Notably, the range of the image brightness adjustment is limited and cannot be infinitely increased or decreased. Furthermore, the brightness adjustment of the image does not affect the gray curve shape, but rather the overall left or right shift (Fig. 2). However, contrast adjustment affects the morphology of the grayscale distribution curve of the image. Therefore, to preserve the original grayscale distribution of

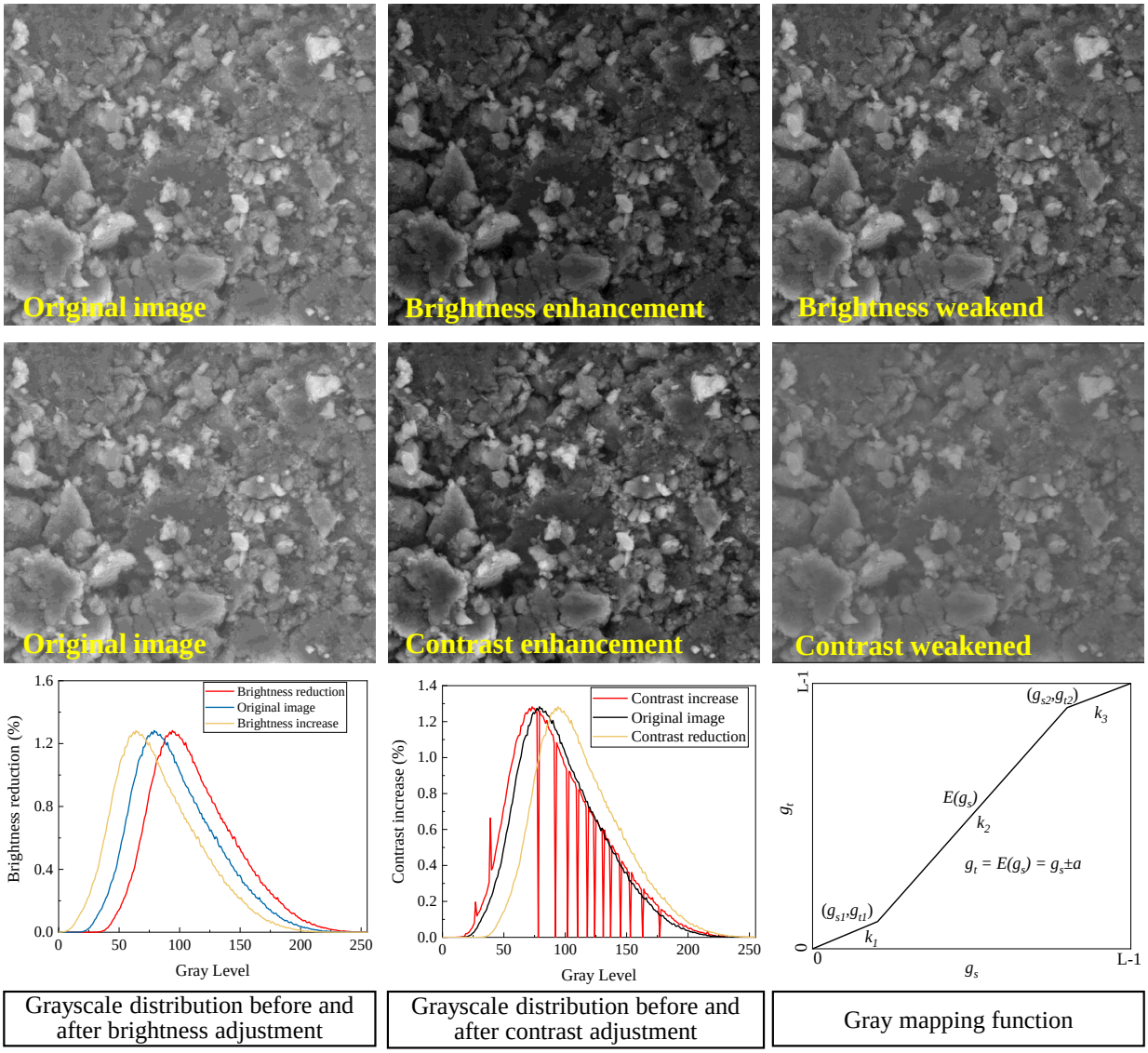

Fig. 2. Effect of image preprocessing on grayscale distribution.

the image, we did not change the contrast of the image during preprocessing. In this study, only the brightness of the image was adjusted within a specified range to obtain the best visual effect such that quantitative characterization would not be significantly affected.

(3) Image denoising

During image acquisition, the quality of the captured image is affected by the environment and equipment. Therefore, appropriate filtering algorithms must be used to reduce image noise (Wang et al., 2021). We compared several typically used noise-removal algorithms (Fig. 3). A mean filter was selected in this study, and an $N \times N$ template was moved across the entire area. The average value ($g(x,y)$) of a certain pixel area was calculated using Eq. (1), which was subsequently used as the gray value of the pixel (Fig. 3):

$$g(x,y) = \frac{1}{N^2} \sum_{(s,t)\in N(x,y)} f(s,t) \tag{1}$$

where $N(x,y)$ corresponds to the $N \times N$ neighborhood of image $f(x,y)$ at position (x,y); $f(x,y)$ is the gray value of the pixel at the position (s,t) of the original image.

(4) Image binarization and porosity calculation

The principle of image binarization is straightforward; that is, by comparing the gray value of each pixel in the image is compared with the selected threshold such that the attributes of the pixel can be determined based on the comparison results (for geomaterials, pores, and matrices):

$$g(x,y) = \begin{cases} 1 & f(x,y) > T \\ 0 & f(x,y) < T \end{cases} \tag{2}$$

where T is the image segmentation threshold and $f(x,y)$ is the gray value of the pixel at the position of the original image. In our previous study, we discovered that a threshold segmentation algorithm based on pixel gradient information is more suitable for bentonite SEM images (Song et al., 2020). Therefore, this algorithm was used for binary image

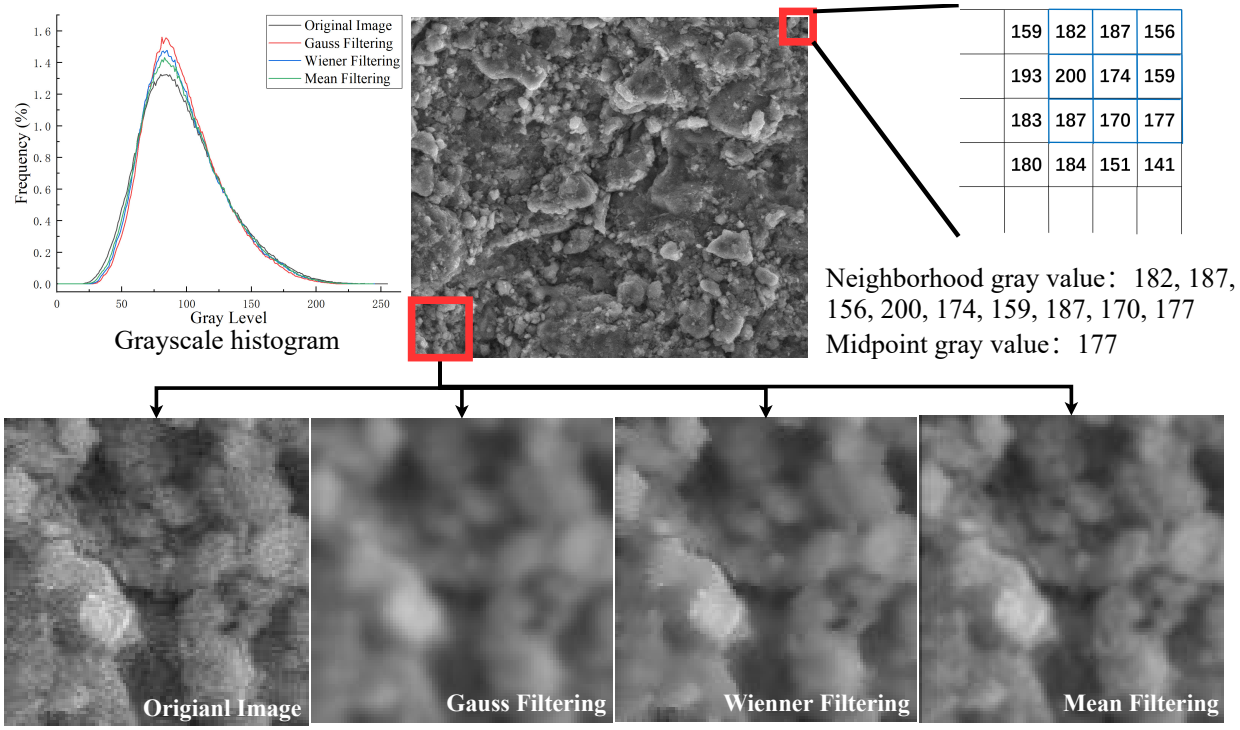

Fig. 3. Principle and schematic diagram of the mean filtering method.

segmentation.

(5) Characterization of pore size distribution

Currently, two types of pore-size distribution algorithms based on digital images are available: discrete pore-size distribution (DPSD) and continuous pore-size distribution (CPSD). In the DPSD algorithm, irregular pores in an image are equated to circles based on the principle of area equivalence. Meanwhile, in the CPSD algorithm, the pores inside a sample and changes in the pore size are assumed to be continuous (Münch and Holzer, 2008). The overall pore interval can be obtained using a circle or sphere with a specific radius to maximize the filling of the internal pore space of the sample and to calculate the filled area or volume. The CPSD method, as schematically shown in Fig. 4 was adopted in this study.

2.1.2 Modified permeability prediction model based on digital images

In this study, gas permeability was calculated based on the pore size distribution obtained above and the Hagen–Poiseuille law as follows:

$$Q = \frac{\pi R^4 \Delta P}{8\mu l} \tag{3}$$

where ΔP is the pressure loss, l the length of the thin tube, μ the dynamic viscosity, Q the flow rate, and R the tube radius.

For a porous medium, the total flow of fluid through the sample and the sum of flows through each minute are considered equal (Fig. 5) as follows:

$$Q = \sum_{i=1}^{n} Q_i \tag{4}$$

where Q_i is the flow rate through each minute pore and n is the number of pipes.

The fluid flow obeys Darcy's law as follows:

$$Q = \frac{kA}{\mu l}\Delta P \tag{5}$$

where k is the permeability and A the cross-sectional area of the fluid. Combining Eqs. (4)-(5):

$$k = \frac{\pi}{8A}\sum R_i^4 = \frac{1}{8A}\sum A_i R_i^2 \tag{6}$$

where R_i is the radius of the pore and A_i the area of the pore with radius R_i.

In Eq. (6), the contribution of the pore size to the seepage characteristics is not considered. Therefore, we modified Eq. (6) and introduced the permeability contribution rate C_i as follows:

$$C_i = \frac{S_i R_i^2}{\sum_{i=1}^{n} S_i R_i^2} \times 100\% \tag{7}$$

where S_i refers to the area occupied by pores with a radius of R_i. Therefore, modifying Eq. (6) yields:

$$k = \frac{1}{8A}\sum_{i=1}^{n} \frac{\pi S_i R_i^6}{\sum_{i=1}^{n} S_i R_i^6} \tag{8}$$

3. Data preparation

3.1 Digital image parameter extraction system

A grayscale image of the surface morphology of GMZ bentonite was obtained, and the grayscale ranged from 0 to 255. The distribution probability ($p(i)$) of the gray value i in

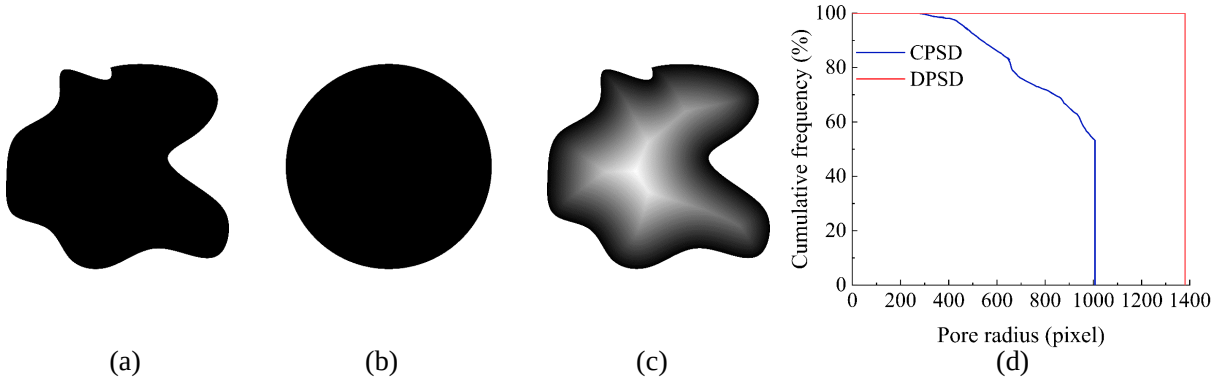

Fig. 4. Schematic diagram of discrete and continuous pore distribution principles: (a) an irregularly shaped pore, (b) a circular pore based on the principle of area equivalence (DPSD), (c) the Euclidian distance map, and (d) a comarision between DPSD and CPSD (Münch and Holzer, 2008; Song et al., 2019).

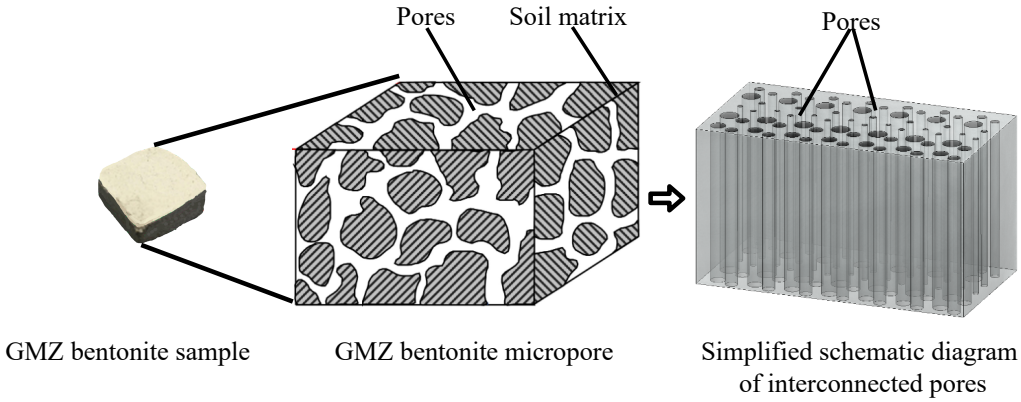

Fig. 5. Permeability prediction model.

the figure is expressed as:

$$p(i)=\frac{n_i}{N_t}, i=0,1,\cdots,L-1 \tag{9}$$

where i represents the gray level, N_t the total number of image pixels, n_i the sum of i pixels in the image, and L the number of gray levels.

The gray mean of the image reflects the average brightness of the entire gray image. A greater gas permeability of the GMZ bentonite implies more pores on its surface, less light reflection, a darker SEM image, and a lower average gray value of the image.

For a normalized grayscale histogram, the gray mean (G) of the image is expressed as:

$$G=\sum_{i=0}^{L-1} ip(i) \tag{10}$$

The grayscale variance (σ^2) of an image reflects the degree of dispersion between the pixel and mean values of the image expressed as follows:

$$\sigma^2=\sum_{i=0}^{L-1}(i-G)^2 p(i) \tag{11}$$

The energy of the image (U) reflects the uniformity of the image gray value expressed as follows:

$$U=\sum_{i=0}^{L-1} p^2(i) \tag{12}$$

Image entropy (E) is a statistical form of features that reflects the average amount of information in an image expressed as:

$$E=-\sum_{i=0}^{L-1} p(i)\log_2 p(i) \tag{13}$$

3.2 ELM system

The ELM algorithm is a feedforward neural networks. The algorithm randomly generates weights and hidden layer thresholds. It does not require adjustments during training and can obtain a unique optimal solution rapidly. Fig. 6 shows the basic structure of the ELM neural network. The connection weight between the input and hidden layers, w, is expressed as follows (see also Fig. 6):

$$w=\begin{bmatrix} w_{11} & w_{12} & \cdots & w_{1n} \\ w_{21} & w_{22} & \cdots & w_{2n} \\ \vdots & \vdots & & \vdots \\ w_{d1} & w_{d2} & \cdots & w_{dn} \end{bmatrix}_{d\times n} \tag{14}$$

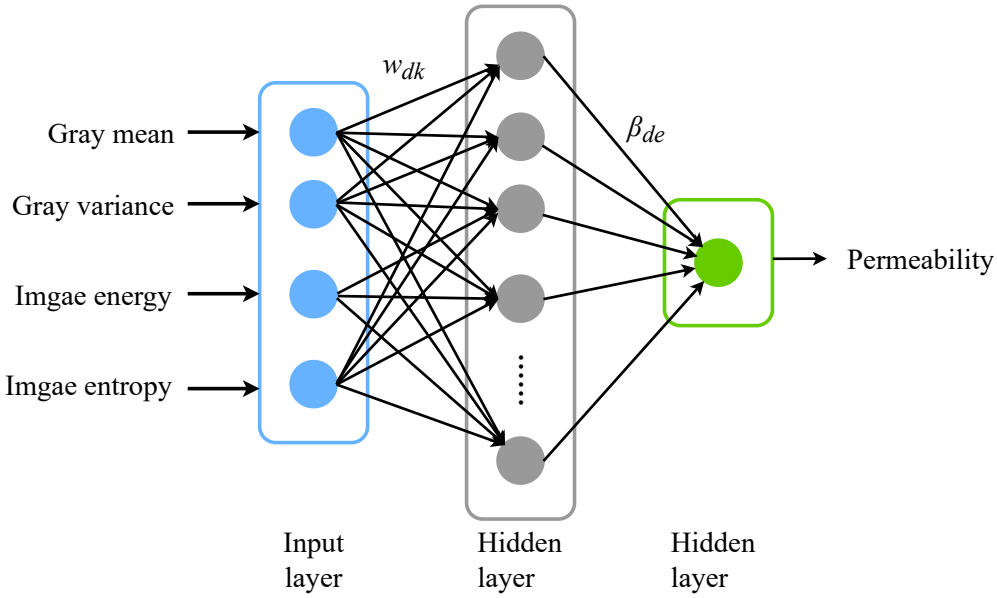

Fig. 6. Structure of the ELM neural network.

Suppose that the connection weight between the hidden and output layers is β, which is expressed as follows:

$$\beta = \begin{bmatrix} \beta_{11} & \beta_{12} & \cdots & \beta_{1m} \\ \beta_{21} & \beta_{22} & \cdots & \beta_{2m} \\ \vdots & \vdots & & \vdots \\ \beta_{d1} & \beta_{d2} & \cdots & \beta_{dm} \end{bmatrix}_{d\times m} \tag{15}$$

Therefore, when the input sample set is Y, the output of the ELM neural network is F, which is expressed as follows:

$$F = \begin{bmatrix} \sum_{i=1}^{d} \beta_{i1} g(w_i x_j + b_i) \\ \sum_{i=1}^{d} \beta_{i2} g(w_i x_j + b_i) \\ \vdots \\ \sum_{i=1}^{d} \beta_{im} g(w_i x_j + b_i) \end{bmatrix}_{m\times 1} \quad (j = 1, 2, \cdots, Y) \tag{16}$$

For any weight w, β, and threshold b, when the number of ELM samples is equal to the number of hidden neurons, the test set approximates the sample value with zero error. In general, the number of hidden neurons is less than that of training samples required to reduce the amount of calculations.

4. Results and discussion

4.1 Training sample construction

Next, training samples were obtained. In theory, a larger number of samples corresponds to more accurate results of the subsequent learning. However, the number of images obtained via SEM in this study was insufficient to construct deep learning samples. To obtain a sufficient number of training samples, we mirrored and folded the original SEM image at each edge and vertex (Figs. 7(a) and 7(b)) and then expanded it to obtain the image shown in Fig. 7(c). Subsequently, we created an 800×800 square labeled with a red dot to signify the center (as shown in Fig. 7(c)) and clipped the corresponding area. The square shifted horizontally and longitudinally in intervals of 40 and stopped at the green point. This sample selection method ensures that the number of samples is multiplied and that the pore information of each sample area is not repeated.

A total of 1,100 SEM images were used in this study. Prior to the scanning, we evaluated the gas permeability of the complete sample (dry state; confining pressure 1 MPa) and obtained 2.3×10^{-15} m^2, which is comparable to the calculation results shown in Fig. 8. However, the permeability results calculated using the digital images differed from those obtained from laboratory tests. Nonetheless, the feasibility of predicting the permeability of porous media based on digital images and deep learning was investigated in this study.

4.2 Relationship between image feature values and permeability

Based on Eqs. (8)-(11) and a set of self-developed systems for extracting feature parameters from SEM images, the relationship between gas permeability and each of the image gray mean, gray variance, image energy, and image entropy can be obtained (Figs. 8(a)-8(d), respectively). However, owing to the extremely discrete data in the graph, linear fitting and regression could not be performed accurately. Hence, a permeability prediction model based on an ELM was established in this study to analyze those data. In this model, multiple image feature parameters were used as input to regress and fit the output of the permeability to realize an accurate permeability prediction.

4.3 ELM model training

To train the model using the ELM gas permeability prediction model, the following steps were implemented:

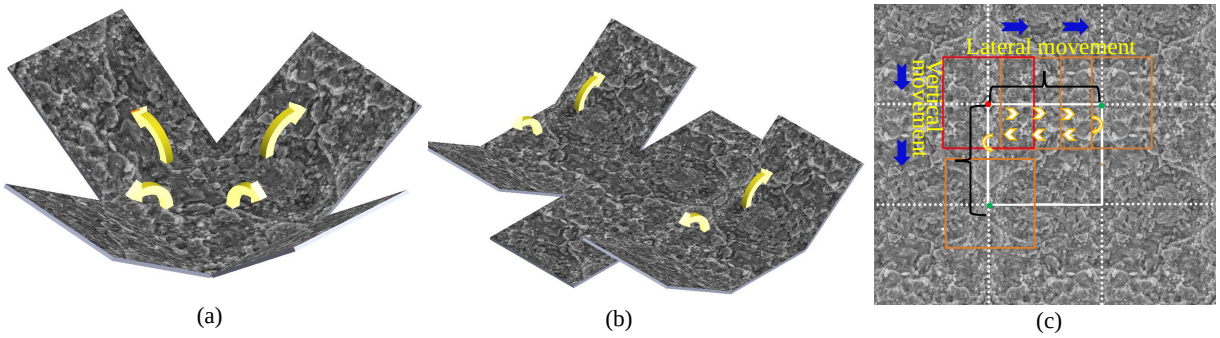

Fig. 7. Illustration of the learning sample construction process: (a) image axis symmetry transformation, (b) image center symmetry transformation, and (c) step-by-step cropping to obtain subsamples.

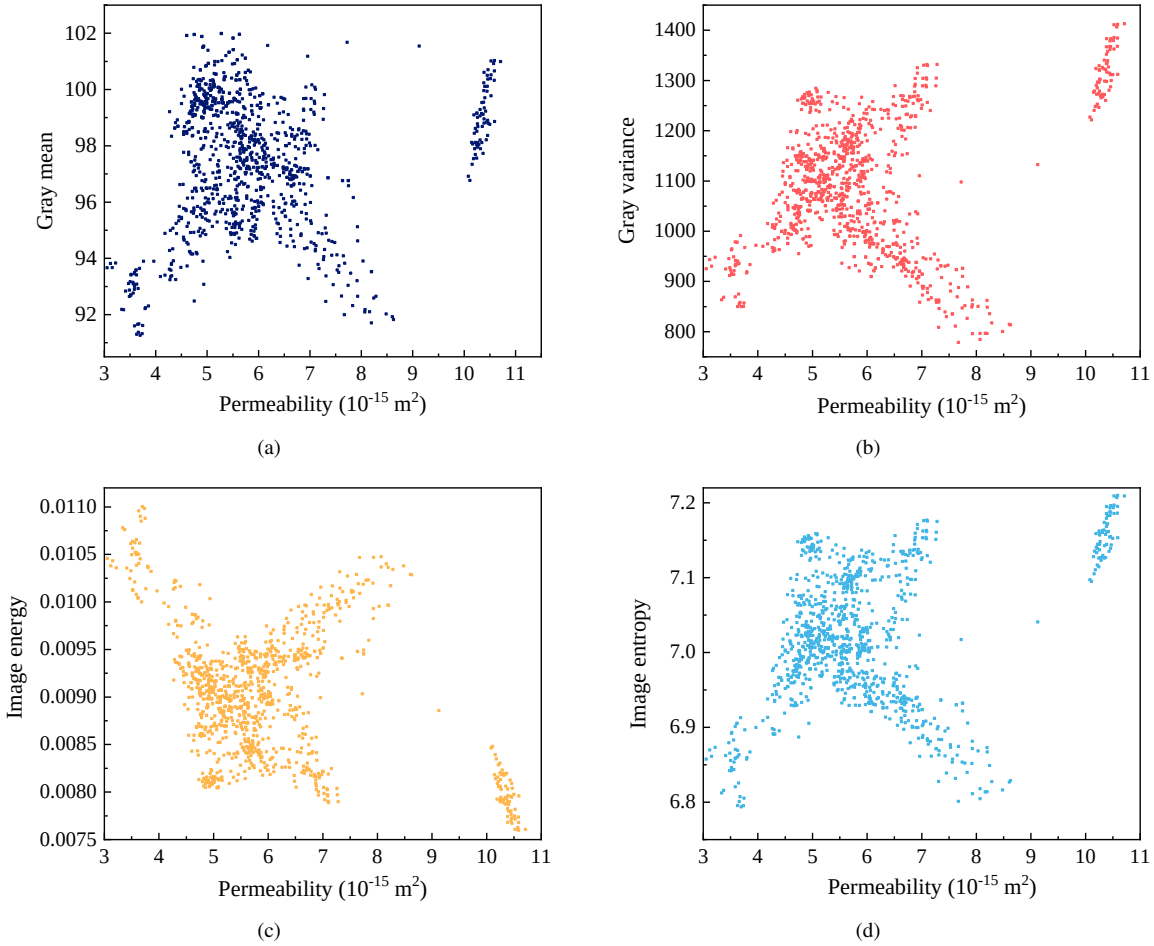

Fig. 8. Relationship between gas permeability and (a) gray mean, (b) gray variance, (c) image energy, and (d) image entropy.

1) A total of 1,100 SEM images of GMZ bentonite corresponding to the gray mean value, gray variance, image entropy value, and image energy composition vector were selected as the input sample. The output value was the permeability corresponding to each SEM image. The ELM neural network contained 1,095 training samples and 5 test samples.
2) The number of neurons in the hidden layer was increased from 1 to 1,000. Five activation functions, namely, "sig", "sin", "hardlim", "radbas" and "radbas" were selected.
3) The mean square error (MSE) of different neuron nodes were calculated for each activation function. Subsequently, the MSE values were compared to determine the optimal activation function and the number of neuron nodes.

To avoid the unpredictable nature of single-time learning outputs and improve the prediction stability of the neural

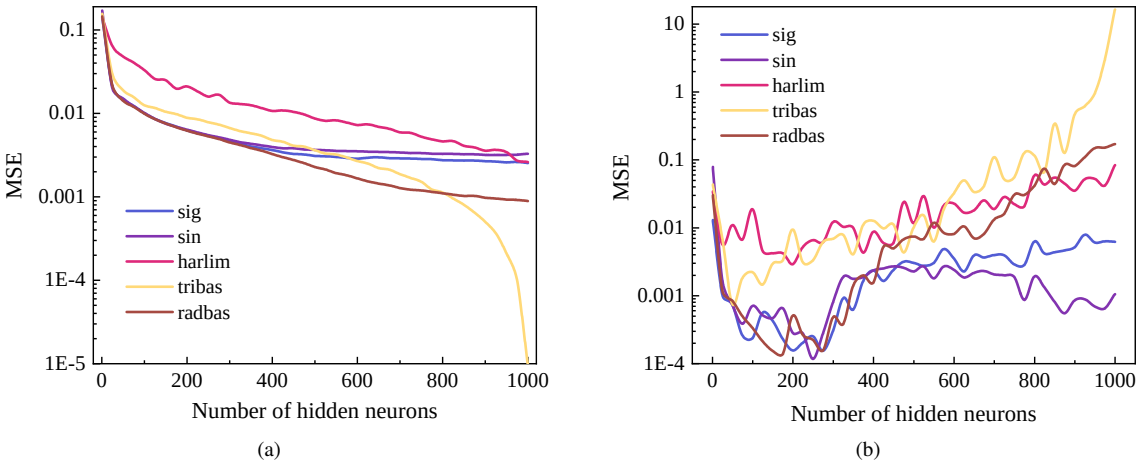

Fig. 9. MSE of different hidden layer nodes for the (a) training and (b) testing samples.

network, the same set of SEM image samples was trained 10 times using the ELM neural network. Subsequently, the average value of 10 MSEs were obtained, as presented in Figs. 9(a) and 9(b), which show the MSEs of the training and testing samples, respectively. During the training and prediction processes, different activation functions and number of neurons affected the calculation results. If an excessive number of neurons is used, then overfitting and unsatisfactory generalization are likely to occur. Therefore, better prediction results can be achieved by simultaneously determining the number of hidden layer neurons and the activation function.

Fig. 9(a) shows that, when the number of neuron nodes is less than 500, the MSE values of the functions are similar, except for the hardlim function. Fig. 9(b) shows that, when the number of neurons is approximately 250, the MSE values of the five activation functions are low. Based on the calculation time (Fig. 10) and the MSE values of the training and test samples, we selected "sin" as the activation function. Meanwhile, the number of neuron nodes was determined to be 250.

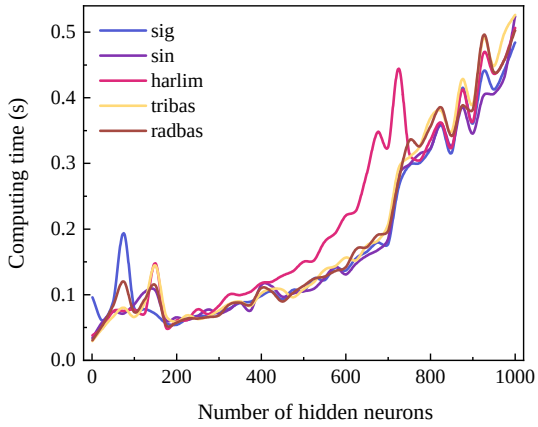

Fig. 10. Computation time for each activation function for different numbers of hidden neurons.

4.4 Results and discussion for the ELM prediction model

After the prediction model was established, five sets of SEM images with unknown permeability were input into the established permeability prediction model. Subsequently, the permeability of those five sets of images was predicted using the ELM neural network model. The prediction was repeated five times to reduce the contingency of model prediction. The results, as presented in Figs. 11(a) and 11(b), show that the prediction is better, except for that of the fourth sample, which indicated a slight deviation. We compiled the statistics for the relative errors of the five sets of images. The average (minimum) errors were 1.50% (0.69%), 8.91% (8.33%), 0.69% (0.04%), 2.06% (0.56%), and 0.95% (0.46%). These values indicate the good adaptability and prediction ability of the model, which can significantly improve the penetration rate prediction and calculation efficiency based on digital images. However, the ELM algorithm must be further improved to achieve more accurate predictions.

In the previous section, we explained that, in addition to the ELM algorithm, several other ML algorithms are typically used, such as SVR, decision tree, and GPR. To compare the prediction results of different algorithms, we used the same training samples as those mentioned above and selected SVR, decision tree, and GPR for training and prediction, as shown in Figs. 12(a) and 12(b). Except for sample No. 2, the results predicted by the ELM algorithm were more similar to the calculated values as compared with those predicted by the other algorithms. In general, the results predicted by the different algorithms did not differ significantly. Meanwhile, the relative error rate of the prediction by the ELM model for each sample was the lowest among the four methods, except for sample No. 2.

The permeability prediction technology based on digital imaging proposed herein can be used for in situ scanning and calculations. Its combination with deep-learning technology can significantly improve the efficiency of calculations and predictions. The prediction accuracy depends on the number and accuracy of training samples. The accuracy of the training samples can be increased by optimizing and improving the

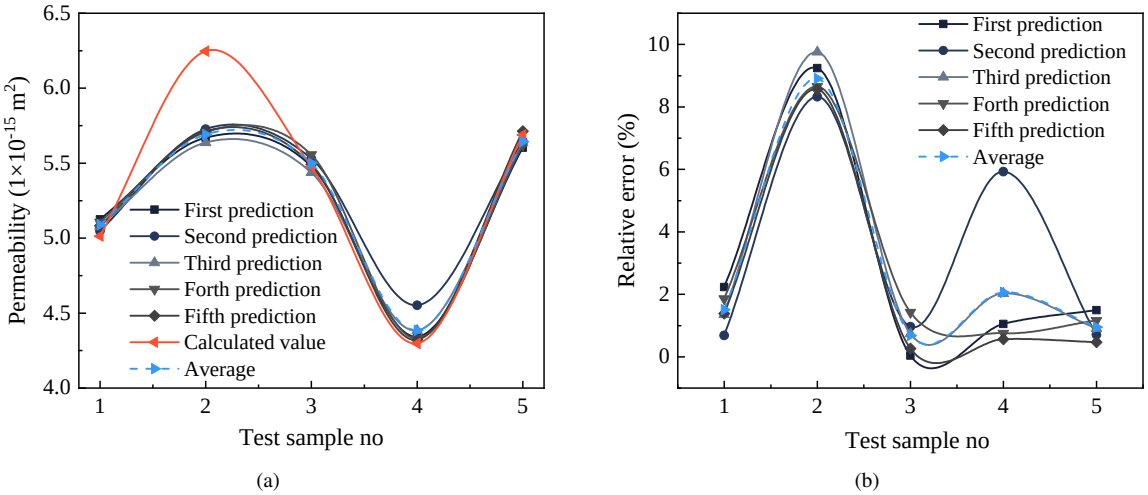

Fig. 11. Permeability prediction based on bentonite SEM images: (a) comparison between predicted and calculated permeability values and (b) relative error of the predicted permeability value.

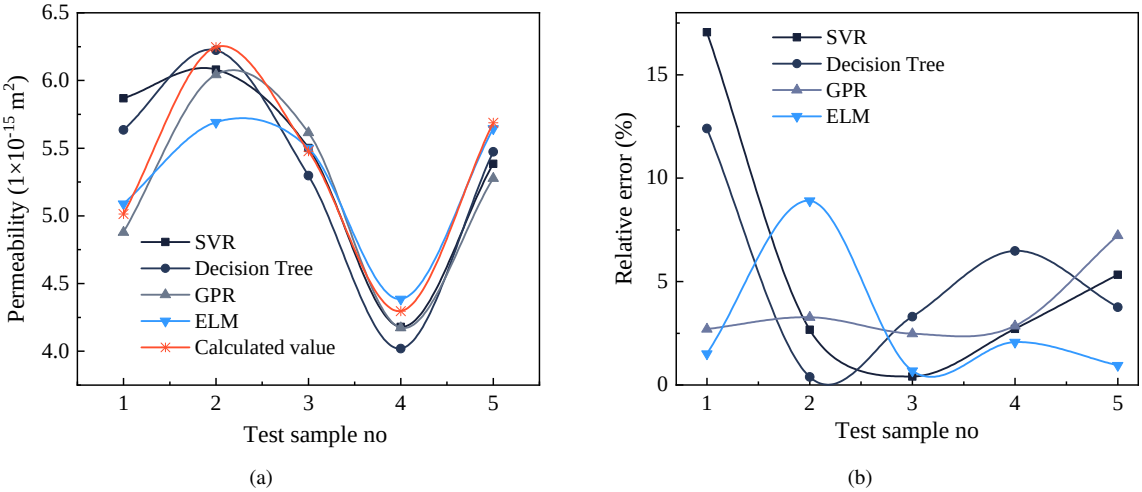

Fig. 12. Permeability prediction based on bentonite SEM images: (a) comparison of the predicted permeability (four different algorithms) and calculated values and (b) relative error of the predicted permeability value.

relevant digital image algorithm.

In this study, permeability prediction and deep learning were conducted on only two-dimensional SEM images. In future studies, the same method can be used for three-dimensional digital images, such as FIB/SEM and CT images, to perform permeability calculation, deep learning, and prediction.

5. Conclusions

Conventional digital image permeability prediction requires a significant amount of time and a complicated calculation process. In this study, digital images were combined with ELM technology to construct a fast and accurate method for predicting permeability. The conclusions are summarized as follows.

First, the training samples were obtained using permeability prediction technology based on digital images. Subsequently, a custom-developed image processing program was used to rapidly obtain four parameters of the image: gray average, gray variance, image energy value, and image entropy. These were core parameters that indicated a relationship with permeability.

To establish an ELM-based permeability learning and prediction system, ELM technology was introduced. A vector composed of the gray mean, gray variance, image energy, and image entropy of an SEM image was used as the input value. Meanwhile, the corresponding permeability value of each SEM image was used as the output value. Multiple adjustments and experiments were performed to determine the appropriate number of neuron nodes and activation functions to achieve the best learning and prediction results.

Permeability prediction based on digital images can be used for in situ scanning and calculations. Combining digital images and ELM technology to establish a permeability

prediction system can significantly improve the calculation and prediction efficiency. Compared with other algorithms, the ELM algorithm offers certain advantages in terms of the accuracy and relative error of prediction. Generally, the prediction results are dependent on the number of training samples and their accuracy, and the accuracy of the training samples can be improved by optimizing and improving the relevant digital image algorithm, which should be investigated in the future.

Acknowledgement

The authors are grateful for the support of the National Natural Science Foundation of China (Nos. 52174133, 51809263), the National Key Research and Development Plan of China (No. 2021YFC2902101) and the Open Found of Key Laboratory of Offshore Geotechnical and Material Engineering of Zhejiang Province (No. OGME21008).

Conflict of interest

The authors declare no competing interest.

References

Ahmadi, R., Shahrabi, J., Aminshahidy, B. Automatic well-testing model diagnosis and parameter estimation using artificial neural networks and design of experiments. Journal of Petroleum Exploration and Production Technology, 2017, 7: 759-783.

Alafnan, S. Utilization of supercritical carbon dioxide for mechanical degradation of organic matters contained in shales. Fuel, 2022, 316: 123427.

Arif, C., Mizoguchi, M., Setiawan, B. I., et al. Estimation of soil moisture in paddy field using artificial neural networks. International Journal of Advanced Research in Artificial Intelligence, 2012, 1: 17-21.

Bahmed, I. T., Khelifa, H., Mohamed, G., et al. Prediction of geotechnical properties of clayey soils stabilised with lime using artificial neural networks (ANNs). International Journal of Geotechnical Engineering, 2019, 13: 191-203.

Carbonell, B., Villar, M. V., Martín, P. L., et al. Gas transport in compacted bentonite after 18 years under barrier conditions. Geomechanics for Energy and the Environment, 2019, 17: 66-74.

Dominguez-Olmedo, J. L., Toscano, M., Mata, J. Application of classification trees for improving optical identification of common opaque minerals. Computers & Geosciences, 2020, 140: 104480.

Dou, W., Liu, L., Jia, L., et al. Pore structure, fractal characteristics and permeability prediction of tight sandstones: A case study from yanchang formation, Ordos Basin, China. Marine and Petroleum Geology, 2021, 123: 104737.

Gebrenegus, T., Ghezzehei, T. A., Tuller, M. Physicochemical controls on initiation and evolution of desiccation cracks in sand–bentonite mixtures: X-ray CT imaging and stochastic modeling. Journal of Contaminant Hydrology, 2011, 126: 100-112.

Hossein, Y., Rasool, K., David, A., et al. Application of mathematical and machine learning models to predict differential pressure of autonomous downhole inflow control devices. Advances in Geo-Energy Research, 2021, 5(4): 386-406.

Huang, J., Zhang, Y., Sun, J., et al. Evaluation of pore size distribution and permeability reduction behavior in pervious concrete. Construction and Building Materials, 2021, 290: 123228.

Mazarei, M., Davarpanah, A., Ebadati, A., et al. The feasibility analysis of underground gas storage during an integration of improved condensate recovery processes. Journal of Petroleum Exploration and Production Technology, 2019, 9: 397-408.

Münch, B., Holzer, L. Contradicting geometrical concepts in pore size analysis attained with electron microscopy and mercury intrusion. Journal of the American Ceramic Society, 2008, 91: 4059-4067.

Shokouhi, P., Kumar, V., PrathiPati, S., et al. Physics-informed deep learning for prediction of CO_2 storage site response. Journal of Contaminant Hydrology, 2021, 241: 103835.

Song, S., Liu, J., Ni, H., et al. A new automatic thresholding algorithm for unimodal gray-level distribution images by using the gray gradient information. Journal of Petroleum Science and Engineering, 2020, 190: 107074.

Song, S., Liu, J., Yang, D., et al. Pore structure characterization and permeability prediction of coal samples based on sem images-sciencedirect. Journal of Natural Gas Science and Engineering, 2019, 67: 160-171.

Taha, O. M. E., Majeed, Z. H., Ahmed, S. M. Artificial neural network prediction models for maximum dry density and optimum moisture content of stabilized soils. Transportation Infrastructure Geotechnology, 2018, 5: 146-168.

Wang, G., Qin, X., Han, D., et al. Study on seepage and deformation characteristics of coal microstructure by 3D reconstruction of CT images at high temperatures. International Journal of Mining Science and Technology, 2021, 31: 175-185.

Xiao, T., Hugh, D. Machine-learning-based object detection in images for reservoir characterization: A case study of fracture detection in shales. Leading Edge, 2018, 37: 435-442.

Xu, L., Ye, W., Chen, Y., et al. Investigation on gas permeability of compacted GMZ bentonite with consideration of variations in liquid saturation, dry density and confining pressure. Journal of Contaminant Hydrology, 2020, 230: 103622.

Zhao, J., Sun, M., Pan, Z., et al. Effects of pore connectivity and water saturation on matrix permeability of deep gas shale. Advances in Geo-Energy Research, 2022, 6(1): 54-68.